https://doi.org/10.1016/j.energy.2019.07.024

Impacts of non-ideal optical factors on the performance of parabolic trough solar collectors

Bin Zou[a, b], Yiqiang Jiang[a, *], Yang Yao[a], Hongxing Yang[b]

[a] School of Architecture, Harbin Institute of Technology; Key Laboratory of Cold Region Urban and Rural Human Settlement Environment Science and Technology, Ministry of Industry and Information Technology, Harbin, China

[b] Renewable Energy Research Group (RERG), Department of Building Services Engineering, The Hong Kong Polytechnic University, Hong Kong, China

Abstract

This work investigated comprehensively the impacts of non-ideal optical factors, including incident angle, sunshape and optical errors on the performance of the parabolic trough collector (PTC). Each optical factor was defined based on their geometrical principles. It was revealed that the heat flux distribution distorted by optical factors was the main cause of changing performance of the PTC. The temperature distribution was completely dependent on the heat flux distribution. The incident angle caused cosine loss and end loss, which respectively reduced the effective incident solar radiation and produced a near-zero heat flux section at one end of the absorber. Based on the effective incident solar radiation, the collector efficiency was reduced by 41.11%

with the incident angle increasing from 0° to 60°. Larger circumsolar ratios produced more uniform circumferential temperature distribution, while reduced greatly the collector efficiency. The specularity error and tracking error affected slightly the receiver's safety, while the slope error reduced obviously the threat to the receiver. When specularity error was small enough (<3 mrad), further improving reflector's specular quality reduced the optical efficiency. The offset direction along X-axis caused the greatest optical loss, and that along positive Y-axis caused local overheating, threatening the receiver's safety.

Keywords: Parabolic trough solar collector; Incident angle; Sunshape; Optical errors; Impacts; Optical and thermal performance

* Corresponding authors: School of Architecture, Harbin Institute of Technology; Key Laboratory of Cold Region Urban and Rural Human Settlement Environment Science and Technology, Ministry of Industry and Information Technology, Harbin, China.

E-mail: jyq7245@163.com (Y. Jiang)

Nomenclature

a	offset angle (°)
A	area (m^2)
b_{sl}	slope error (mrad)
b_{tr}	tracking error (mrad)
c_1, c_2, c_μ	constants in turbulence model
c_p	specific heat at constant pressure
d	diameter (m)
e	relative deviation (%)
f	friction factor
f_c	focal length (m)
f_P	friction factor calculated by empirical formula
F_i	mass force components (N)
h	heat transfer coefficient ($W/m^2 \cdot K$)
k	pulsation kinetic energy
I_D	direct normal solar radiation intensity (W/m^2)
I_{eff}	effective solar radiation intensity (W/m^2)
l_a	offset distance (m)
L_c	length of the used PTC module (m)
m	mass flow rate (kg/s)
Nu	Nusselt number
Nu_G	Nusselt number calculated by empirical formula
p	pressure (Pa)
q_{loss}	heat loss (W)
q_u	useful energy obtained by the HTF (W)
Re	Reynolds number
T	temperature (K)

ΔT	circumferential temperature difference (K)
u_i	velocity components, i=1, 2, 3 (m/s)
V	velocity (m/s)
W_c	aperture width of the PTC module (m)
x_A	abscissa of any point A on the reflector

Greek symbols

α_a	absorptivity of the selective coating
δ	radial angle of the solar disk (δ=4.65mrad)
δ_Δ	maximum radial angle of the Buie's model (δ_Δ=43.6mrad)
δ_{ij}	Kronecker delta
ε	turbulent dissipation rate
ε_{coa}	emittance of the selective coating
η	efficiency (%)
η_c	collector efficiency of the PTC (%)
η_o	optical efficiency (%)
η_t	thermal efficiency of the receiver tube (%)
θ_{in}	incidence angle (mrad)
θ_s	radial angle of the point on the sun (mrad)
θ_{sp}	the deviation of the reflected beam from the specular direction (mrad)
λ	thermal conductivity (W/m·K)
μ	dynamic viscosity (Pa·s)
μ_t	turbulence viscosity (Pa·s)
ρ	density (kg/m^3)
ρ_r	reflectivity of the reflector
σ_ε	Prandtl number for turbulent dissipation rate
σ_k	Prandtl number for turbulent kinetic energy
σ_{sl}	standard deviation of slope error (mrad)

σ_{sp}	standard deviation of specularity error (mrad)
σ_t	turbulence Prandtl number
τ_g	transmissivity of the glass envelope
φ_a	circle angle of the absorber (°)

Subscripts

a	absorber
amb	ambient
ave	average
f	fluid
g	glass envelope
i	inner surface
in	inlet
max	maximum
min	minimum
o	outer surface
out	outlet
s	simulation
t	test
x, *y*, *z*	Cartesian coordinates

Abbreviations

CFD	computational fluid dynamics
CSP	concentrating solar power
CSR	circumsolar ratio
FVM	Finite Volume Method
HTF	heat transfer fluid
MCRT	Monte Carlo Ray Tracing
PTC	parabolic trough solar collector

UDF	User Defined Functions

1. Introduction

As the most cost-effective and developed technology in concentrating solar power (CSP) area, the parabolic trough solar collector (PTC) technology has been applied worldwide [1-3]. The PTC is a typical kind of linear solar concentrator consisting mainly of a parabolic reflector and a receiver tube that is composed of a glass envelope and a metal absorber tube. For high temperature generation, the annulus between the glass envelope and the absorber tube is maintained vacuum to reduce heat loss and avoid oxidation of the selective coating. The incident sunrays are focused onto the absorber tube by the parabolic reflector and absorbed by the selective coating, and subsequently transferred to the heat transfer fluid (HTF) flowing inside the tube. Due to the nature of the rays concentration of the reflector, the heat flux distribution around the absorber is non-uniform [4, 5], which increases the complexity of the thermal performance of the receiver tube.

Over decades, numerous studies have be conducted to investigate or improve the performance of the PTCs [3, 6]. Jeter [4, 5] developed an integral model for calculating the energy flux on the absorber surface. His findings have usually been used for model validation by other researchers [7, 8]. Grena [9, 10] adopted a ray tracing recursive algorithm to investigate the optical performance and further discussed the efficiency gain with an infrared-reflective film on the non-radiation part of the receiver. Khanna et al. [11] developed analytical expressions for flux distribution on a bent absorber tube and further validated their optical models by experimental results [12]. Liang et al. [13]

compared three optical models and proposed a novel coupled method by combining the advantages of those models. In recent years, the Monte Carlo Ray Tracing (MCRT) method was widely adopted to study the optical characteristics of concentrating solar collectors [8, 14-16], which was proved to be accurate and flexible. There were also many studies performed on PTCs' thermal performance [17]. Although typical tests [18-20] and some experiments [21-23] were carried out, numerical simulation was still the major method used for investigating the thermal performance of the PTC [24]. Forristall [25] compared one-dimensional and two-dimensional heat transfer models implemented by Engineering Equation Solver (EES) and proposed that the accuracy of the two-dimensional model was higher than that of the one dimensional model as the length of the receiver was more than 100 m. Hachicha et al. [7] developed a geometrical-numerical model to simulate the heat transfer in the receiver tube under condition of non-uniform heat flux. Their models were validated against analytical results [4, 5] and testing results [18]. Padilla et al. [26] conducted a simulation on the heat transfer of the PTC based on a one-dimensional model, and compared the results with experimental data and other simulated results. Kalogirou [27] developed a detailed thermal model which involved all the heat transfer forms in the receiver and was solved in EES. Yang et al. [28] proposed a dynamic three-dimensional volume element model which combined the laws of thermodynamics and heat transfer as well as empirical correlations to simplify the modeling. In order to simulate the thermal performance under non-uniform heat flux distribution, MCRT coupled with computational fluid dynamics (CFD) method was usually used for investigating the photo-thermal coupling process of the PTC system [29-35].

In practice, there are various non-ideal factors, such as non-zero incident angle, uneven sunshape and optical errors including specularity error, slope error, tracking error and absorber alignment error. Due to the deflecting and scattering effects of non-ideal factors, the heat flux distribution on the absorber surface is strikingly distorted, which leads to changing optical and thermal performance of the PTC. However, previous researches have seldom examined comprehensively the influences of non-ideal optical factors on the performance of the PTC. Most studies were usually performed with an assumption of uniform solar disk or no optical errors. As for the thermal performance, researchers mainly focused on the heat transfer modeling and corresponding enhancement measures [17, 35], while the non-ideal optical factors were usually neglected. Although some studies discussed indeed the optical factors, most of them emphasized partially only one or two types of the optical errors [36-38], and the others usually convolved all the optical errors together as a Gaussian approximation model [39, 40] which, in fact, cannot reflect the essence and loses the geometrical and spatial dependence of optical errors [41]. Therefore, this study aims to investigate comprehensively the impacts of all the non-ideal optical factors on the performance of the PTC based on the individual characterization of each optical factor. The heat flux distribution calculated by MCRT was added to the FLUENT code as the boundary condition using the User Defined Functions (UDF). Detailed discussions were conducted on the optical and thermal performance of the PTC under different optical factors. Some useful findings were presented, which can be used as the reference for structural design and optimization.

2. Description of optical factors

2.1 Incident angle

In practice, due to the limitation of single-axis tracking mode, the non-zero incident angle is inevitably caused. As Fig. 1 shows, the incident angle (θ_{in}) is defined as the angle between the incident rays and the transverse section that is perpendicular to the focal line. Due to the non-zero incident angle, the effective solar radiation intensity (I_{eff}) incident on the collector aperture, compared with the direct normal solar radiation intensity (I_D), is reduced, which is defined as the cosine loss. In addition, one end of the absorber tube cannot receive any reflected sunrays, and some rays escape from the other side of the PTC (as shown in Fig. 1), which is defined as end loss. The effective solar radiation intensity caused by the cosine loss is calculated by Eq. (1).

$$I_{eff} = I_D \cdot \cos\theta_{in} \tag{1}$$

The length of the absorber that cannot receive reflected sunrays from any point A on the reflector, caused by the end loss, can be calculated by Eq. (2).

$$\Delta L_{\mathrm{A}} = \mathrm{HF} = \mathrm{AH} \cdot \tan\theta_{in} = \left(x_{\mathrm{A}}^2 / 4 f_c + f_c \right) \cdot \tan\theta_{in} \tag{2}$$

2.2 Effective sunshape

Because of the limb darkening and atmospheric attenuation scattering, the radiation intensity distribution on the solar image obtained on earth is uneven [42, 43], as shown in Fig. 2. Buie et al. [44] developed a generic sunshape model based on the vast data collected by the Lawrence Berkeley Laboratories (LBL) and the German Aerospace Center (DLR). In their model, the solar profile was divided into two parts: the solar disk with a radial angle of 4.65 mrad and the aureole which was produced by the small angle forward scattering caused by the solar beam interacting with

atmospheric particles. The most important parameter in their model was the circumsolar ratio (CSR) which was defined as the ratio of the energy contained within the aureole to the total energy contained in both the solar disk and aureole. In Buie's model, the brightness at any point was normalized against the central intensity and given by Eq. (3) [44].

$$\phi(\theta_s)=\begin{cases}\dfrac{\cos(0.326\theta_s)}{\cos(0.308\theta_s)} & \theta_s \le 4.65\ \text{mrad}\\ e^{\kappa}\theta_s^{\gamma} & \theta_s > 4.65\ \text{mrad}\end{cases} \tag{3}$$

where θ_s is the radial angular displacement (radial angle) of any point on the sun, κ and γ are given by Eq. (4) and Eq. (5) respectively [44].

$$\kappa = 0.9\log(13.5\chi)\chi^{-0.3} \tag{4}$$

$$\gamma = 2.2\log(0.52\chi)\chi^{0.43} - 0.1 \tag{5}$$

where χ is the circumsolar ratio (i.e. CSR) and given by Eq. (6).

$$\chi = \frac{2\pi\int_{\delta}^{\delta_\Delta}\phi(\theta_s)\sin(\theta_s)d\theta_s}{2\pi\int_{0}^{\delta_\Delta}\phi(\theta_s)\sin(\theta_s)d\theta_s} \tag{6}$$

where δ and δ_Δ are the radial angular size of the solar disk (δ =4.65mrad) and the upper limit of the circumsolar region respectively.

The specularity error refers to the non-specular reflection property caused by the imperfect microscopic texture of the reflector. With the specularity error, the solar radiation in the reflected optical cone will be redistributed, forming a reflected sunshape that is different from the incident sunshape. In this study, the reflected sunshape was defined as the effective sunshape. According to Refs. [45, 46], the specularity error of the reflector can be expressed as the Gaussian distribution, and given by Eq. (7).

$$R(\theta_{sp}) = \frac{1}{\sqrt{2\pi}\sigma_{sp}} \exp\left(-\frac{\theta_{sp}^2}{2\sigma_{sp}^2}\right) \tag{7}$$

where σ_{sp} is the standard deviation of the specularity error distribution.

Therefore, according to mathematical theory, the effective sunshape model after reflection can be developed by convolving the incident sunshape model (i.e. Eq. (3)) with the specularity error model (i.e. Eq. (7)), and given by Eq. (8).

$$\phi_{eff}(\theta_s) = \int_{-\delta_\Delta}^{\delta_\Delta} \phi(\theta') R(\theta_s - \theta') d\theta' \tag{8}$$

2.3 Optical errors

In actual system, there are other three main types of optical errors which are slope error, tracking error and absorber alignment error. Slope error (b_{sl}) is the angular deviation of the actual surface normal direction from the ideal normal direction. Generally, the slope error is not constant over the reflector surface and can be measured in practice [41, 47]. Note that an angular deviation of the surface normal vector causes twice the angular deviation of the reflected rays. Since no measured data can be used, the slope error in this study was generated by Gaussian model, and given by Eq. (9).

$$R(b_{sl}) = \frac{1}{\sqrt{2\pi}\sigma_{sl}} \exp\left(-\frac{b_{sl}^2}{2\sigma_{sl}^2}\right) \tag{9}$$

where σ_{sl} is the standard deviation of the slope error distribution.

Tracking error (b_{tr}) is the angle between the plane containing the vertex and the focal line and the plane containing the focal line and the sun. It is determined by the accuracy of the tracking system and does not change with the points on the reflector. For any point on the reflector, the slope error and the tracking error just deflect the entire incident optical cone by a certain angle ($2b_{sl}$ and b_{tr}) without changing the

sunshape. Thus, in the MCRT programing, it only need to add (or subtract) these two optical errors to the original direction without convolving with the incident sunshape, which was completely different from the treatment of the specularity error presented above.

Absorber alignment error is defined as the deviation of the absorber tube from the focal line of the parabolic reflector. It is usually specified by two parameters: the offset distance (l_a) and the offset angle (a). For more clarity, Fig. 3 shows the geometric description of the slope error, tracking error and the absorber alignment error. Note that the parameter φ_a in Fig. 3 is the circumferential angle of absorber, which will be used to characterize the circumferential heat flux and temperature distribution on the absorber outer surface in later sections.

3. Modeling and validation

3.1 MCRT model

Monte Carlo Ray Tracing (MCRT) method is a powerful tool for calculating the circumferential heat flux distribution under any optical conditions. It initializes the position and the direction of the incident sunrays according to the sunshape model and determines the optical actions, including reflection, transmission and absorption, based on a series of randomly generated numbers. The propagating path of each ray is traced and the landing position on the absorber's outer surface is recorded accordingly to produce the statistical results of the heat flux distribution. More detailed information about MCRT was elaborated in the authors' previous study [15]. The flowchart of MCRT is given in Fig. 4.

3.2 Flow and heat transfer model

3.2.1 Governing equations

The governing equations of continuity, momentum and energy can be given by Eq. (10) ~ Eq. (12).

Continuity equation:

$$\frac{\partial\left(\rho u_i\right)}{\partial x_i}=0 \tag{10}$$

Energy equation:

$$\frac{\partial\left(\rho c_p T u_i\right)}{\partial x_i}=\frac{\partial}{\partial x_i}\left[\left(\lambda+\frac{\mu_t}{\sigma_t}\right)\frac{\partial T}{\partial x_i}\right] \tag{11}$$

Momentum equation:

$$\frac{\partial\left(\rho u_i u_j\right)}{\partial x_j}=-\frac{\partial p}{\partial x_i}+\frac{\partial}{\partial x_j}\left[\left(\mu+\mu_t\right)\left(\frac{\partial u_i}{\partial x_j}+\frac{\partial u_j}{\partial x_i}\right)-\frac{2}{3}\left(\mu+\mu_t\right)\frac{\partial u_i}{\partial x_i}\delta_{ij}-\frac{2}{3}\rho k\delta_{ij}\right]+\rho F_i \tag{12}$$

The standard k - ε model is used to perform turbulence calculation, which includes the k equation and the ε equation, as given by Eq. (13) and Eq. (14) respectively.

k equation:

$$\frac{\partial\left(\rho k u_i\right)}{\partial x_i}=\frac{\partial}{\partial x_i}\left[\left(\mu+\frac{\mu_t}{\sigma_k}\right)\frac{\partial k}{\partial x_i}\right]+G_k-\rho\varepsilon \tag{13}$$

ε equation:

$$\frac{\partial\left(\rho\varepsilon u_i\right)}{\partial x_i}=\frac{\partial}{\partial x_i}\left[\left(\mu+\frac{\mu_t}{\sigma_\varepsilon}\right)\frac{\partial k}{\partial x_i}\right]+c_1\frac{\varepsilon}{k}G_k-c_2\rho\frac{\varepsilon^2}{k} \tag{14}$$

where the turbulence viscosity (μ_t) and the generation rate of k (G_k) are given by Eq. (15) and Eq. (16) respectively.

$$\mu_t = c_\mu \rho \frac{k^2}{\varepsilon} \tag{15}$$

$$G_k = \mu_t \frac{\partial u_i}{\partial x_j}\left(\frac{\partial u_i}{\partial x_j} + \frac{\partial u_j}{\partial x_i}\right) \tag{16}$$

The constants in the turbulence model are listed in Table 1 [48].

3.2.2 Boundary conditions

The boundary conditions were set as following: (1) Inlet: mass flow inlet, $m_z=m_{in}$, $m_x=m_y=0$, $T=T_{in}$, $k_{in}=1\%\cdot 0.5\rho u_x^2$, $\varepsilon_{in}=c_\mu \rho k_{in}^2/\mu_t$ [48]; outlet: fully developed condition; (2) No-slip boundary condition was applied to all solid walls; (3) The heat flux was calculated by the MCRT and added to the absorber outer surface using UDF; (4) The radiation between the absorber outer surface and the glass inner surface was calculated by the Surface to Surface (S2S) model; (5) The outer surface of the glass cover was set as mixed boundary condition including convection between the surface and the ambient, and radiation between the surface and the sky. The heat transfer coefficient between the glass envelope outer surface and the ambient is calculated by Eq. (17) [49], and the sky temperature was viewed as 8K lower than the ambient temperature [25]. The emittance of the glass envelope was 0.86 [25]. The selective coating was the Luz Cermet, and its emittance in the temperature range between 300 K and 700 K was given by Eq. (18) [25].

$$h_{g-amb} = 4V_{amb}^{0.58} d_{g,o}^{-0.42} \tag{17}$$

$$\varepsilon_{coa} = 0.000327 \times T - 0.065971 \tag{18}$$

3.2.3 Solution method

The flow and heat transfer simulation was conducted using the FLUENT codes which were developed based on the FVM. A MCRT program for calculating the heat

flux distribution was developed, and read by the FLUENT software as the boundary condition of the absorber outer surface. The SIMPLE algorithm was adopted to ensure the coupling of pressure and velocity. The governing equations were discretized by second order upwind scheme. The standard wall function was used to deal with the flow and heat transfer in near-wall region. Two criteria were used to guarantee the convergence of the solution: the maximum residual for energy equation and radiation equation were less than 10^{-6}, and the fluid outlet temperature remained constant for the last 1000 iterations.

3.2.4 Performance assessment parameters

Several important parameters were used to evaluate the performance of the PTC, as given as follows:

As Table 3 shows, the specific heat (c_p) is linearly dependent on temperature (T). Thus, the useful energy obtained by the HTF (q_u) can be calculated by:

$$q_u = m \cdot \frac{c_{p,in} + c_{p,out}}{2} \cdot \left(T_{out} - T_{in}\right) \tag{19}$$

Optical efficiency (η_o):

$$\eta_o = \frac{q_u + q_{loss}}{I_{eff} \cdot W_c \cdot L_c} \tag{20}$$

According to Eq. (1), it is easily found that the denominator of Eq. (20) is the effective total energy incident on the reflector caused by the cosine effect. Thus, the optical efficiency in this study just reflects the effects of end loss.

The thermal efficiency of the receiver tube (η_t):

$$\eta_t = \frac{q_u}{q_u + q_{loss}} \tag{21}$$

The collector efficiency of the PTC (η_c):

$$\eta_c = \eta_o \cdot \eta_t \tag{22}$$

3.3 Grid independence checking and model validation

The PTC prototype used in this study is the SEGS LS-2 PTC which has been tested in the AZTRAK rotating platform by Sandia National Laboratories [18]. Some main parameters of the SEGS LS-2 PTC are listed in Table 2. The HTF used in Sandia test was Syltherm 800, the thermal property parameters of which were temperature-dependent and given in Table 3 [50]. Six typical cases were selected from Ref. [18] for validation of the established models, as given in Table 4.

3.3.1 Grid independence checking

The number of grid cells should be determined by considering both the results' precision and the computing time. The structured grids were adopted in this study, and the total number of the cells was determined by setting respectively the number of the nodes in the circumferential, radial and axial direction. The fluid outlet temperature (T_{out}), the average Nusselt number (Nu_{ave}) and the average friction factor (f_{ave}) were used for grid independence checking. Nu_{ave} and f_{ave} are calculated by Eq. (23) and Eq. (24) respectively.

$$Nu_{ave} = \frac{q_u}{A_{a,i}\left(T_{a,i} - T_f\right)} \times \frac{d_{a,i}}{\lambda} \tag{23}$$

$$f_{ave} = \frac{2\left(p_{in} - p_{out}\right) d_{a,i}}{\rho V^2 L} \tag{24}$$

Taking case 1 from Table 4 as the representative, the results for grid independence checking were given in Table 5. It is clearly that when the number of cells was more

than 72×40×400 (circumferential × radial × axial), the results of T_{out}, Nu_{ave} and f_{ave} were all almost kept constant. Therefore, the meshing of 72×40×400 will be used in this study. The schematic of domain discretization (meshing) of the receiver tube was shown in Fig. 5.

3.3.2 Model validation

The established models will be validated by comparing the outlet temperature of the HTF between the simulation ($T_{out,s}$) and the test ($T_{out,t}$) under the conditions presented in Table 4. The relative deviation (e_T) of the outlet temperature is defined by Eq. (25).

$$e_T = \frac{\left|T_{out,s} - T_{out,t}\right|}{\left|T_{out,t} - T_{in}\right|} \times 100\% \tag{25}$$

The comparison results were given in Table 6 which showed that the simulation results agreed well with the test results. The maximum relative deviation of the outlet temperature was 10.29% and the average relative deviation was 9.1%, indicating that the established models can simulate well the actual flow and heat transfer process of the receiver tube.

In Sandia test, a solid plug was inserted concentrically in the absorber tube to ensure large velocity. In this study, the solid plug was removed, which is more practical. In order to further validate the applicability of the established models in simulation in the hollow tube, the obtained results of Nu_{ave} and f_{ave} were compared with that calculated by the classical empirical formulas proposed respectively by Gnielinski [51] and Petukhov [52]. The two formulas were given by Eq. (26) and Eq. (27) respectively.

$$Nu_G = \frac{(f/8)(Re-1000)Pr_f}{1+12.7(f/8)^{1/2}\left(Pr_f^{2/3}-1\right)}\left[1+\left(\frac{d_{a,i}}{L_a}\right)^{2/3}\right]\left(\frac{Pr_f}{Pr_{a,i}}\right)^{0.11} \quad (26)$$

$$f_P = \left[1.82\log_{10}(Re)-1.64\right]^{-2} \quad (27)$$

It is clearly seen from Fig. 6 that the simulation results were in good accordance with the results calculated by the empirical formulas. As the mass flow rate increased from 1 kg/s to 8 kg/s, the maximum relative deviations of Nu and f were 6.32% and 10.28% respectively, and the average relative deviations were only 5.44% and 2.27% respectively, validating the reliability of the established models.

4. Results and discussion

The study was performed under the following conditions: the incident solar radiation intensity was 1000 W/m^2; the inlet temperature of HTF was 573.15 K; the mass flow rate was 1 kg/s; the ambient temperature was 293.15 K; the wind velocity was 2 m/s. The absorptance (α_a), the reflectance (ρ_r) and the transmittance (τ_g) were all assumed as constants.

4.1 Impacts of incident angle

Fig. 7 shows the variation of heat loss (q_{loss}) and each efficiency (η) with the incident angle (θ_{in}). It is clearly seen from the figure that q_{loss} deceased from 1683 W to 1253 W with θ_{in} increasing from 0° to 60°. This is because the cosine loss and the end loss increased by increasing θ_{in} reduce the heat flux on the absorber surface and lower the absorber temperature. It can also be seen from the figure that η_t dropped from 94.91% to 85.98%, dropping by 8.93% as θ_{in} increased from 0° to 60°. The possible reason is that the absorber temperature lowered by the larger cosine and end loss increases the viscosity of the HTF, weakening the turbulence and hence decreasing

the heat transfer. Fig. 7 also shows that η_o deceased obviously from 84.85% to 45.86%, dropping by 38.99%, with θ_{in} increasing from 0° to 60°. This indicates that, according to Eq. (20), the end loss causes great optical loss. Because of the weakening of both the optical efficiency (η_o) and the thermal efficiency (η_t) of the receiver tube, the collector efficiency (η_c) of the PTC decreased consistently with the increase of θ_{in}. As θ_{in} increased from 0° to 60°, η_t decreased from 80.54% to 39.43%, dropping by 41.11%.

Given that the heat flux distribution along the longitudinal direction (Z-axis) is uneven under non-zero incident angle, two longitudinal sections (i.e. *z*=2 m and *z*=7.5 m) were selected as representatives for analysis. Fig. 8 shows the circumferential heat flux distribution on the absorber outer surface at *z*=2 m and *z*=7.5 m under different incident angles (θ_{in}). It can be seen from Fig. 8 that when θ_{in} was less than 30°, the heat flux distribution at the two sections (i.e. *z*=2 m and *z*=7.5 m) were the same, and the heat flux decreased with increasing θ_{in}. The reason is that when θ_{in} was less than 30°, both the two sections can receive all the reflected rays from the entire aperture width (i.e. the end loss does not affect the flux distribution at those two sections), and larger θ_{in} causes larger cosine loss, hence decreasing the heat flux. Whereas, when θ_{in} was equal to 45°, the heat flux at *z*=2 m dropped significantly and the high flux area shrank obviously, compared with that at *z*=7.5 m. In particular, when θ_{in} increased to 60°, the heat flux at the bottom part of the absorber was zero. The reason is shown in Fig. 9 which displays the variation of the end loss (ΔL_{A}) with the absolute value of abscissa of point A ($|x_{\mathrm{A}}|$) under different incident angles (θ_{in}) based on Eq. (2).

Note that since the aperture width of the LS-2 PTC is 5 m (given in Table 2), the maximum of $|x_A|$ was set as 2.5. It can be easily found from Fig. 9 that when θ_{in} was less than 30°, ΔL_A was always smaller than 2 m for any $|x_A|$, indicating that the section at z=2 m can receive all the reflected rays from the entire aperture width in this case (i.e. not affected by the end loss). When θ_{in} was 45°, only the reflected rays from the points with $|x_A|$ less than 1.2 m can be received by the absorber at z=2 m, which reduces remarkably the heat flux on the absorber tube. As θ_{in} was 60°, ΔL_A for all the points in the reflector width was larger than 2 m (the minimum was 3.19 m), which means that all the reflected rays from the reflector aperture cannot be received by the absorber at z=2 m in this case. Therefore, the heat flux at the bottom of the absorber at z=2 m was zero for θ_{in}=60°, as shown in Fig. 8(a). From Fig. 9, it can also be found that the ΔL_A for all the discussed incident angles were always smaller than 7.5 m (the maximum was only 4.5 m), which means that the section with z=7.5 m can receive all the reflected rays from the entire aperture for any incident angle discussed (0°~60°). Thus, the heat flux distribution at z=7.5 m is only affected by the cosine loss. As Fig. 8(b) shows, due to the increase of cosine loss, the high heat flux decreased consistently with the increase of incident angle. It can also be found from Fig. 8(b) that the angle span of the high flux area increased with the increase of θ_{in}. This is because the distance of the reflected rays from the reflector to the absorber (i.e. AF in Fig. 1) becomes larger as θ_{in} increases, producing a larger solar image on the outer surface of the absorber. It can be expected from Fig. 9 that there exists a incident angle threshold, more than which the whole absorber cannot receive any reflected rays (i.e. $\Delta L_A \geq L_c$),

causing the maximum end loss. As a matter of fact, according to Eq. (2), the minimum incident angle that causes the maximum end loss for the LS-2 PTC was 77°. Fig. 10 shows the circumferential temperature distribution on the absorber outer surface at z=2 m and z=7.5 m under different incident angles (θ_{in}). It is clearly seen from the figure that the temperature distribution was similar to the heat flux distribution, and the temperature corresponds exactly to the intensity of the heat flux, which is in line with the actual situation.

In order to display the heat flux distribution and temperature distribution more intuitively and clearly, the color maps are presented in Fig. 11 and Fig. 12 respectively. It is easily found from Fig. 11 that when θ_{in} was not zero, there was a section of absorber at one end which cannot receive any reflected rays, forming a near-zero heat flux section and its length increases consistently with the increase. Fig. 11 also shows that the color of the high flux area (i.e. bottom part of the absorber) faded with the increase of θ_{in}, demonstrating that the high heat flux declines with increasing θ_{in}, which is the same as what presented in Fig. 8. This is because the larger incident angle increases the cosine loss, hence decreasing the heat flux. The temperature distribution was similar to the heat flux distribution, as shown in Fig. 12, and there was a section of low temperature absorber tube corresponding to the near-zero heat flux section shown in Fig. 11. Because of the increasing cosine loss, the temperature at the position with the same z coordinate decreased (color faded) with the increase of θ_{in}, showing the same variation trend as the heat flux.

Fig. 13 shows the variation of the maximum and minimum temperature and the maximum circumferential temperature difference at z=7.5 m with the incident angle for

the absorber tube and the glass envelope. Since the effective solar radiation intensity was reduced by the cosine loss, both the maximum and minimum temperature of the absorber tube decreased with increasing θ_{in}, as shown in Fig. 13(a). The drop of the maximum temperature ($T_{a,max}$) of the absorber was much larger than the minimum temperature ($T_{a,min}$). Consequently, the maximum circumferential temperature difference of the absorber ($\Delta T_{a,max}$) decreased obviously with the increase of θ_{in}. As the θ_{in} increased from 0° to 60°, $\Delta T_{a,max}$ decreased from 100.4 K to 53.6 K, dropping by 46.8 K. This is because the weakening effect of the cosine loss on the heat flux reduces significantly the absorber temperature. From Fig. 13(b), it can be found that the temperature of the glass envelope was much smaller than that of the absorber due to the outstanding insulation capability of the vacuum annulus. The variation trends of the glass envelope temperature was the same as that of the absorber. This is because the glass envelope receives heat from the absorber. As the θ_{in} increased from 0° to 60°, $\Delta T_{g,max}$ decreased from 18.8 K to 9.3 K, dropping by 9.5 K. Given the fact that the variation trend of the glass envelope temperature is the same as the absorber, only the absorber temperature distribution will be discussed in the later sections. It can be concluded from above discussion that the incident angle causes cosine loss and end loss, which reduce the received energy remarkably and, also, decrease obviously the circumferential temperature gradient.

4.2 Impacts of effective sunshape

As mentioned above, the reflected effective sunshape was produced by convolving the incident sunshape model (i.e. Buie's model) with the specularity error model. Thus the effects of the effective sunshape depend on both the CSR and the specularity error

(σ_{sp}), which will be discussed in detail in this part.

4.2.1 Impacts of incident sunshape

In this section, the specularity error was 3 mrad (σ_{sp}=3 mrad) and other optical errors were zero. Given that the heat flux distribution along the absorber was uniform under the condition of θ_{in}=0°, the section with *z*=7.5 m was used as the example for analysis in following study. Fig. 14 shows the variation of heat loss (q_{loss}) and each efficiency (η) with the circumsolar ratio (CSR). It is clearly seen from Fig. 14 that q_{loss} declined from 1677 W to 1585 W, dropping only by 92 W, and the drop of η_t was only 0.5%, as CSR increased from 0 to 0.7. This demonstrates that the CSR has little impact on the heat transfer performance of the receiver tube. Whereas, the optical performance was weakened obviously by increasing CSR. As Fig. 14 shows, the η_o decreased from 84.32% to 72.48%, dropping by 11.84%, with CSR rising from 0 to 0.7. This is because larger CSR increases the energy distribution in the circumsolar region, causing more sunrays escaping from both sides of the absorber (i.e. intercept factor reduced). The variation of η_c was similar to that of η_o, dropping from 80.01% to 68.41% with CSR increasing from 0 to 0.7.

Fig. 15 shows the circumferential heat flux and circumferential temperature distribution on the absorber outer surface at *z*=7.5 m under different circumsolar ratios (CSRs). It is obviously seen from Fig. 15(a) that the high flux area was widened and the peak heat flux was reduced with the increase of CSR, demonstrating that larger CSR produces more uniform heat flux distribution. The reason is that more solar energy is distributed in the circumsolar area and the radiation intensity at the central region of the

solar disk is reduced as the CSR increases, producing more uniform solar profile. From Fig. 15(b), it can be observed that the distribution of the circumferential temperature of the absorber was similar to that of the heat flux, indicating that the temperature distribution was completely determined by the heat flux distribution. Fig. 15(b) also shows that the maximum temperature ($T_{a,\max}$) of the absorber decreased with the increase of CSR due to the decrease of the peak heat flux, while the minimum temperature ($T_{a,\min}$) of the absorber varied little, which indicates that the influence of the CSR is mainly reflected in weakening the high temperature. Consequently, the maximum circumferential temperature difference ($\Delta T_{a,\max}$) of the absorber declined with the increase of CSR. When the CSR increased from 0 to 0.7, $\Delta T_{a,\max}$ decreased from 99.5K to 84.3K, demonstrating larger CSRs reduce the threat to the receiver tube.

4.2.2 Impacts of specularity error

The CSR used in this section was 0.1 and other optical errors were zero. Fig. 16 shows the variation of heat loss (q_{loss}) and each efficiency (η) with the specularity error (σ_{sp}). It can be observed from Fig. 16 that q_{loss} decreased from 1671 W to 1620 W, dropping only by 51 W, and the η_t almost remained stable with σ_{sp} increasing from 1 mrad to 9 mrad, demonstrating that the influence of σ_{sp} on the heat transfer performance of the receiver tube is negligible in practice. However, the σ_{sp} affected the optical performance of the PTC remarkably. As Fig. 16 shows, the η_o grew slightly firstly and then declined quickly with the increase of σ_{sp}. This indicates that although improving the specular quality of the reflector is an effective way to improve the PTC's performance, it is not necessary to improve the quality to a very high degree

(σ_{sp}<3 mrad). As the η_t of the receiver tube remained almost stable, the η_c of the collector presented the same variation trend as the η_o. When σ_{sp} increased from 1 mrad to 9 mrad, the η_c rose slightly from 79.19% to 79.46% firstly, and then dropped obviously to 73.33%.

Fig. 17 shows the circumferential heat flux and circumferential temperature distribution on the absorber outer surface at *z*=7.5 m under different specularity errors (σ_{sp}). It can be clearly seen from Fig. 17(a) that the heat flux distribution became more homogenous and the peak heat flux decreased continuously with the increase of σ_{sp}. This is because larger σ_{sp} scatters more reflected rays to a larger angle span of the reflected optical cone, producing a more uniform reflected solar profile. Fig. 17(a) also shows that in the high heat flux area of the absorber tube, part of the heat flux was reduced and the other was increased with the increase of σ_{sp}. This phenomenon is more obvious when σ_{sp} was less than 5 mrad. As the figure shows, when σ_{sp} was less than 5 mrad, the heat flux in the circle angle range between -60° and -30° (also between 30° and 60°) decreased with the increase of σ_{sp}, whereas that in the range between -30° and 30° was increased with increasing σ_{sp}. This indicates that when σ_{sp} is small (<5 mrad), the increment of σ_{sp} plays the role of cutting peaks and filling valleys in the high flux area. This is also the reason for the slight growth of the optical efficiency with specularity error increasing in a small value range (shown in Fig. 16). As discussed previously, the variation trend of the circumferential temperature distribution on the absorber outer surface was the same as that of the circumferential heat flux distribution. It can be seen from Fig. 17(b) that when σ_{sp} was smaller than

5 mrad, the maximum temperature ($T_{a,\max}$) of the absorber was almost kept stable because of the effect of cutting peaks and filling valleys of the σ_{sp}. Afterwards, $T_{a,\max}$ decreased with the increase of σ_{sp}. The minimum temperature ($T_{a,\min}$) of the absorber remained almost constant for all the σ_{sp}, demonstrating that the effect of σ_{sp} on the low temperature area is negligible. The maximum circumferential temperature difference ($\Delta T_{a,\max}$) of the absorber showed the same variation property as the $T_{a,\max}$, and its drop was only about 7.1 K as σ_{sp} increased from 1 mrad to 9 mrad. Therefore, the influences of the specularity error on the safety and stability of the receiver tube are negligible in practice.

4.3 Impacts of optical errors

The optical errors discussed in this part were slope error, tracing error and absorber alignment error, which were all generated at the macro level. The CSR and σ_{sp} used in this part were 0.1 and 5 mrad respectively.

4.3.1 Impacts of slope error

Fig. 18 shows the variation of heat loss (q_{loss}) and each efficiency (η) with the slope error (σ_{sl}). As shown in the figure, when σ_{sl} increased from 1 mrad to 5.5 mrad, the drop of q_{loss} and η_t were 104 W and 0.65% respectively, which reveals that the impacts of σ_{sl} on the heat transfer performance of the receiver tube is not obvious. The optical performance was weakened remarkably by increasing σ_{sl}. It can be found from Fig. 18 that η_o was reduced from 82.93% to 68.95%, dropping by 13.98%, as σ_{sl} increased from 1.5 mrad to 5.5 mrad. This is because larger slope errors lead to greater deviation of the actual surface normal direction from the ideal normal direction,

causing more incident sunrays reflected away from the ideal reflection direction. The variation of the η_c of the collector was the same as that of the η_o. As σ_{sl} increased from 1.5 mrad to 5.5 mrad, the η_c decreased from 78.67% to 64.96%, dropping by 13.71%.

Fig. 19 shows the circumferential heat flux and circumferential temperature distribution on the absorber outer surface at *z*=7.5 m under different slope errors (σ_{sl}). Obviously, the high heat flux was reduced and the flux distribution became more uniform as the σ_{sl} increased. The reason is that, for the entire reflector, more dispersed solar radiation will be produced because of reflected sunrays deviated more away from the ideal direction caused by larger slope errors. In particular, the high-intensity radiation at the center of the solar disk can be reflected to the sides of the absorber tube to a greater extent by the larger slope errors, consequently reducing the heat flux at the bottom of the absorber pipe. Meanwhile, more reflected rays escape from both sides of the absorber tube (i.e. intercept factor reduced), causing overall decrease of the heat flux. The circumferential temperature distribution was similar to the heat flux distribution, as shown in Fig. 19(b). It can be found from Fig. 19(b) that $T_{a,\max}$ decreased from 686.5 K to 666.5 K, dropping by 20 K, while $T_{a,\min}$ dropped only by 2.1 K, as σ_{sp} increased from 1.5 mrad to 5.5 mrad. This demonstrates that the slope error mainly affects the high temperature distribution. The $\Delta T_{a,\max}$ decreased from 97.8K to 80.2K, dropping by 17.6K, with σ_{sp} increasing from 1.5 mrad to 5.5 mrad.

4.3.2 Impacts of tracking error

Fig. 20 shows the variation of heat loss (q_{loss}) and each efficiency (η) with the tracking error (b_{tr}). It can be seen from the figure that the drop of the q_{loss} and the η_t was only 54 W and 0.3% respectively with b_{tr} increasing from 1 mrad to 9 mrad, revealing that the tracking error has little influence on the heat transfer of the receiver tube. In contract, the optical performance was reduced greatly by the tracking error. As Fig. 20 depicts, the η_o dropped obviously from 83.47% to 76.45% as b_{tr} increased from 1 mrad to 9 mrad. As a result, the η_c of the collector had the same variation trend as the η_o. When b_{tr} increased from 1 mrad to 9 mrad, the η_c decreased from 79.16% to 72.28%, dropping by 6.88%.

Fig. 21 shows the circumferential heat flux and circumferential temperature distribution on the absorber outer surface at *z*=7.5 m under different tracking errors (b_{tr}). It is clearly seen from the Fig. 21(a) that the left peak heat flux was larger than the right one and the heat flux curves moved overall toward the right side of φ_a=0° which is the opposite side of the b_{tr} (left side shown in Fig. 3). This indicates that the tracking error destroys the symmetry of the heat flux distribution and more energy will be distributed on the opposite direction of the tracking error. Fig. 21(a) also shows that the angle span of the high flux area changed little as the b_{tr} increased from 1 mrad to 9 mrad. Thus, the heat transfer performance of the receiver tube will also not change much, as shown in Fig. 20. As with previous analyses, the circumferential temperature distribution was similar to the circumferential heat flux distribution, as shown in Fig. 21(b). It can be clearly found from Fig. 21(b) that both $T_{a,\max}$ and $\Delta T_{a,\max}$ dropped only by 6.6 K as

the b_{tr} increased from 1 mrad to 9 mrad. This demonstrates that the influences of the tracking error on the safety of the receiver tube are negligible.

4.3.3 Impacts of absorber alignment error

This section takes the case of l_a =0.02 m as an example to investigate the influences of the offset angle (a) on the PTC's performance. Given the symmetry of the parabola, the range of the offset angle discussed in this study was between -90° and 90°. Fig. 22 shows the variation of heat loss (q_{loss}) and each efficiency (η) with the offset angle (a). As the figure shows, the q_{loss} increased firstly and then dropped with the increase of a. The maximum difference of q_{loss} and the maximum drop of the η_t was only 62 W and 0.2% respectively, indicating that the offset angle has little effects on the receiver tube's heat transfer performance. When a was 0°, the η_o was the minimum, demonstrating that the offset direction along the X-axis causes the greatest optical loss. Note that the offset distance discussed in this study was only 0.02 m (i.e. l_a =0.02 m). It can be expected that as the offset distance increased further, the variation range of the optical efficiency will be larger. Due to the stability of the η_t, the variation trend of the η_c was the same as that of the η_o. The minimum η_c obtained at a=0° was 75.12%.

Fig. 23 shows the circumferential heat flux and circumferential temperature distribution on the absorber outer surface at *z*=7.5 m under different offset angles (a). It can be easily seen from Fig. 23(a) that the angle span of the high heat flux area shrank and the peak heat flux increased continuously with a increasing from -90° to 90°, worsening the non-uniformity of the heat flux distribution. From Fig. 23(a), it can also

be found that when the a was not ±90°, the heat flux curves moved towards the opposite side of the a (right side shown in Fig. 3). As Fig. 23(b) shows, the distribution of the temperature was similar to the heat flux. As a varied from -90° to 90°, the maximum temperature ($T_{a,\max}$) of the absorber grew from 656.4 K to 741.5 K, increasing remarkably by 85.1 K. The rise of the maximum circumferential temperature difference ($\Delta T_{a,\max}$) was also obvious (more than 87 K). It can be concluded that the offset direction along positive Y-axis causes the greatest uneven temperature distribution and is most likely to result in local overheating on the absorber tube surface, which should be avoided in practice.

4.4 Summary of results

This part presented a summary of the effects of each optical factor on the performance parameters of the PTC for clear and convenient assessment and comparison, and the results were given in Table 7.

Table 7 Summary of the results

Optical factors		Value range	Drop of performance parameters				
			q_{loss}	η_o	η_t	η_c	$\Delta T_{a,max}$
θ_{in}		0° ~ 60°	430W	38.99%	8.93%	41.11%	46.8K
Effective sunshape	CSR	0 ~ 0.7 σ_{sp}=3mrad	92W	11.84%	0.5%	11.6%	15.2K
	σ_{sp}	1 ~ 9mrad CSR=0.1	51W	6%	0.23%	5.86%	7.1K
CSR=0.1 σ_{sl}=5mrad	σ_{sl}	1.5 ~ 5.5mrad	104W	13.98%	0.65%	13.71%	17.6K
	b_{tr}	1 ~ 9mrad	54W	7.02%	0.3%	6.88%	6.6K
	a	-90° ~ 90°	62W	0.94%	0.2%	0.88%	Maximum at

	l_a=0.02m	Minimum at a=0°	Minimum at a=0°	a=90° Raised by 87K
Remarks	1) Optical Efficiency was calculated based on effective solar radiation (cosine effect). 2) Effects of the alignment error will be more obvious for larger offset distances. 3) Impacts of optical factors were mainly reflected in weakening the optical efficiency.			

5. Conclusions

This work carried out a detailed study on the impacts of non-ideal optical factors, including non-zero incident angle, sunshape, and optical errors, on the optical and thermal performance of the PTC. All the optical factors discussed were characterized clearly based on their geometrical and generation principles. The performance of the PTC, including heat loss, optical and thermal efficiencies, heat flux and temperature distribution, and the circumferential temperature difference under different optical factors were discussed in detail. Some conclusions can be drawn as follows:

(1) The temperature distribution is completely dependent on the heat flux distribution. Due to the outstanding insulation of the vacuum annulus, the glass envelope temperature is much smaller than the absorber, and has the same variation trend as the absorber temperature. All the discussed optical factors have little effects on the heat transfer in the receiver tube, whereas influence remarkably the optical performance. The heat flux distribution changed by optical factors affects greatly the thermal performance and the reliability of the receiver tube.

(2) The non-zero incident angle causes cosine loss and end loss, which reduces significantly the effective received energy and, also, decreases obviously the circumferential temperature. As the incident angle increased from 0° to 60°, the collector efficiency which was defined based on the effective solar radiation intensity,

decreased from 80.54% to 39.43%, dropping by 41.11%. Due to the end loss, a near-zero heat flux section is formed at one end of the absorber, the length of which increases with increasing incidence angle.

(3) Larger CSRs produce more uniform circumferential temperature distribution, while reduce the collector efficiency obviously. The influences of the specularity error and tracking error on the uniformity of the absorber temperature are slight, while the slope error reduces the circumferential temperature gradient obviously. The collector efficiency is reduced significantly by increasing the slope error or tracking error. It is not necessary to improve the specular quality of the reflector to a very high degree, due to efficiency reduction caused by small specularity errors (σ_{sp} <3 mrad).

(4) The absorber alignment error has great impacts on the circumferential temperature distribution. The offset direction along X-axis causes the greatest optical loss for the same offset distance. The offset direction along positive Y-axis causes the greatest uneven temperature distribution and is most likely to result in local overheating on the absorber tube surface, which should be avoided in practice.

Acknowledgements

This work was supported by the National Key R&D Program of China (Project Number: 2017YF0702604).

References

[1] Price H, Lupfert E, Kearney D, Zarza E, et al. Advances in parabolic trough solar power technology. Journal of Solar Energy Engineering 2002; 124: 109-125.

[2] Schiel W. Collector development for solar parabolic trough power plants. Bautechnik 2012; 89: 182-191.

[3] Wang FQ, Cheng ZM, Tan JY, Yuan Y, et al. Progress in concentrated solar power technology with parabolic trough collector system: A comprehensive review. Renewable and Sustainable Energy Reviews 2017; 79: 1314-1328.

[4] Jeter SM. Calculation of the concentrated flux density distribution in parabolic trough collectors by a semifinite formulation. Solar Energy 1986; 37: 335-345.

[5] Jeter SM. The distribution of concentrated solar radiation in paraboloid collectors. Journal of Solar Energy Engineering 1986: 108: 219-225.

[6] Kumaresan G, Sudhakar P, Santosh R, Velraj R. Experimental and numerical studies of thermal performance enhancement in the receiver part of solar parabolic trough collectors. Renewable and Sustainable Energy Reviews 2017; 77: 1363-1374.

[7] Hachicha AA, Rodríguez I, Capdevila R, Oliva A. Heat transfer analysis and numerical simulation of a parabolic trough solar collector. Applied Energy 2013; 111: 581-592.

[8] Cheng ZD, He YL, Wang K, Du BC, et al. A detailed parameter study on the comprehensive characteristics and performance of a parabolic trough solar collector system. Applied Thermal Engineering 2014; 63: 278-289.

[9] Grena R. Optical simulation of a parabolic solar trough collector. International Journal of Sustainable Energy 2010; 29: 19-36.

[10] Grena R. Efficiency Gain of a solar trough collector due to an ir-reflective film on the non-irradiated part of the receiver. International Journal of Green Energy 2011; 8: 715-733.

[11] Khanna S, Kedare SB, Singh S. Analytical expression for circumferential and axial distribution of absorbed flux on a bent absorber tube of solar parabolic trough

concentrator. Solar Energy 2013; 94: 26-40.

[12] Khanna S, Sharma V, Kedare SB, Singh S. Experimental investigation of the bending of absorber tube of solar parabolic trough concentrator and comparison with analytical results. Solar Energy 2016; 125: 1-11.

[13] Liang HB, You SJ, Zhang H. Comparison of three optical models and analysis of geometric parameters for parabolic trough solar collectors. Energy 2016; 96: 37-47.

[14] Cheng ZD, He YL, Cui FQ. A new modelling method and unified code with MCRT for concentrating solar collectors and its applications. Applied Energy 2013; 101: 686-698.

[15] Zou B, Dong JK, Yao Y, Jiang YQ. A detailed study on the optical performance of parabolic trough solar collectors with Monte Carlo Ray Tracing method based on theoretical analysis. Solar Energy 2017; 147: 189-201.

[16] H. Hoseinzadeha, A. Kasaeianb, M.B. Shafii. Geometric optimization of parabolic trough solar collector based on the local concentration ratio using the Monte Carlo method. Energy Conversion and Management 2018; 175: 278-287.

[17] Conrado LS, Rodriguez-Pulido A, Calderon G. Thermal performance of parabolic trough solar collectors. Renewable and Sustainable Energy Reviews 2017; 67: 1345-1359.

[18] Dudley V, Kolb G, Sloan M, Kearney D. SEGS LS2 solar collector–test results. Report of Sandia National Laboratories, Albuquerque, NM, USA, 1994; SANDIA 94-1884.

[19] Burkholder F, Kutscher C. Heat-loss testing of Solel's UVAC3 parabolic trough receiver. NREL Technical Report, 2008; NREL/TP-550-42394.

[20] Burkholder F, Kutscher C, Heat loss testing of Schott's 2008 PTR70 parabolic trough receiver. NREL Technical Report, 2009; NREL/TP-550-45633.

[21] Lei DQ, Li Q, Wang ZF, Li J, et al. An experimental study of thermal characterization of parabolic trough receivers. Energy Conversion and Management 2013; 69: 107-115.

[22] Zou B, Dong JK, Yao Y, Jiang YQ. An experimental investigation on a small-sized parabolic trough solar collector for water heating in cold areas. Applied Energy 2016; 163: 396-407.

[23] Lu JF, Yuan QY, Ding J, Wang WL, et al. Experimental studies on nonuniform heat transfer and deformation performances for trough solar receiver. Applied Thermal Engineering 2016; 109: 497-506.

[24] Yilmaz IH, Soylemez MS. Thermo-mathematical modeling of parabolic trough collector. Energy Conversion and Management 2014; 88: 768-784.

[25] Forristall R. Heat transfer analysis and modelling of a parabolic trough solar receiver implemented in engineering equation solver. 2003; NREL/TP-550-34169.

[26] Padilla RV, Demirkaya G, Goswami DY, Stefanakos E, et al. Heat transfer analysis of parabolic trough solar receiver. Applied Energy 2011; 88: 5097-110.

[27] Kalogirou S. A detailed thermal model of a parabolic trough collector receiver. Energy 2012; 48: 298-306.

[28] Yang S, Sensoy TS, Ordonez JC. Dynamic 3D volume element model of a parabolic trough solar collector for simulation and optimization. Applied Energy 2018; 217: 509-526.

[29] Wirz M, Roesle M, Steinfeld A. Three-dimensional optical and thermal numerical

model of solar tubular receivers in parabolic trough concentrators. Journal of Solar Energy Engineering 2012; 134: 041012-1–2-9.

[30] He YL, Xiao J, Cheng ZD, Tao YB. A MCRT and FVM coupled simulation method for energy conversion process in parabolic trough solar collector. Renewable Energy 2011; 36: 976-985.

[31] He YL, Cheng ZD, Cui FQ, Li ZY. Numerical investigations on a pressurized volumetric receiver: solar concentrating and collecting modelling. Renewable Energy 2012; 44: 368-379.

[32] Cheng ZD, He YL, Cui FQ, Xu RJ, et al. Numerical simulation of a parabolic trough solar collector with nonuniform solar flux conditions by coupling FVM and MCRT method. Solar Energy 2012; 86: 1770-1784.

[33] Wu ZY, Li SD, Yuan GF, Lei DQ, et al. Three-dimensional numerical study of heat transfer characteristics of parabolic trough receiver. Applied Energy 2014; 113: 902-911.

[34] Liang HB, Fan M, You SJ, Zheng WD, et al. A Monte Carlo method and finite volume method coupled optical simulation method for parabolic trough solar collectors. Applied Energy 2017; 201: 60-68.

[35] Sandeep HM, Arunachala UC. Solar parabolic trough collectors: A review on heat transfer augmentation techniques. Renewable and Sustainable Energy Reviews 2017; 69: 1218-1231.

[36] Cheng ZD, He YL, Cui FQ, Du BC, et al. Comparative and sensitive analysis for parabolic trough solar collectors with a detailed Monte Carlo ray-tracing optical model. Applied Energy 2014; 115: 559-572.

[37] Zhao D, Xu E, Wang Z, Yu Q, Xu L, et al. Influences of installation and tracking errors on the optical performance of a solar parabolic trough collector. Renewable Energy 2016; 94: 197-212.

[38] Mwesigye A, Huan Z, Bello-Ochende T, Meyer JP. Influence of optical errors on the thermal and thermodynamic performance of a solar parabolic trough receiver. Solar Energy 2016; 135: 703-718

[39] Bendt P, Rabl A, Gaul HW, Reed KA. Optical Analysis and Optimization of Line-focus Solar Collectors. Solar Energy Research Institute, Golden, CO, 1979, pp. 1-64, SERI/TR 34-092.

[40] Thomas A, Guven HM. Effect of optical errors on flux distribution around the absorber tube of a parabolic trough concentrator. Energy Conversion and Management 1994; 35: 575-582.

[41] Zhu GD, Lewandowski A. A new optical evaluation approach for parabolic trough collectors: first-principle optical intercept calculation. Journal of Solar Energy Engineering 2012; 134: 041005-1-8.

[42] Neumann A, Schubnell M. Irradiance and sunshape measurements for the Cologne site, In: Proceedings of the 8th International Solar Forum, 1992, pp. 1173-1183.

[43] Neumann A, Witzke A, Jones SA, Schmitt G. Representative terrestrial solar brightness profiles. Journal of Solar Energy Engineering 2002; 124: 198-204.

[44] Buie D, Monger AG, Dey CJ. Sunshape distributions for terrestrial solar simulations. Solar Energy 2003; 74: 113-122.

[45] Cooper T, Steinfeld A. Derivation of the angular dispersion error distribution of mirror surfaces for monte carlo ray-tracing applications. Journal of solar energy

engineering 2011; 133: 044501-1-4.

[46] Pettit RB. Characterization of the reflected beam profile of solar mirror materials. Solar Energy 1977; 19: 733-741.

[47] Ulmer S, Heinz B, Pottler K, Lupfert E. Slope error measurements of parabolic troughs using the reflected image of the absorber tube, Journal of Solar Energy Engineering 2009; 131: 011-014.

[48] Tao WQ. Numerical Heat Transfer (2nd Edition). Xi'an Jiaotong University Press, Xi'an; 2001.

[49] Mullick SC, Nanda SK. An improved technique for computing the heat loss factor of a tubular absorber. Solar Energy 1989; 42: 1-7.

[50] Agustin MD-T, Lourdes G-R. Comparison of solar technologies for driving a desalination system by means of an Organic Rankine Cycle. Desalination 2007; 216: 276-291.

[51] Gnielinski V. New equations for heat and mass transfer in turbulent pipe and channel flow. International Chemical Engineering 1976; 16: 359-368.

[52] Petukhov BS. Heat Transfer and Friction in Turbulent Pipe Flow with Variable Physical Properties. Advances in Heat Transfer 1970; 6: 503-564.

Figures:

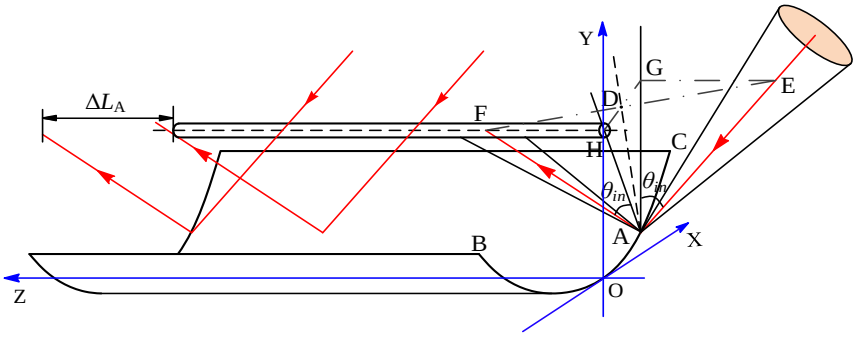

Fig. 1 Schematic of the incident angle and the end loss

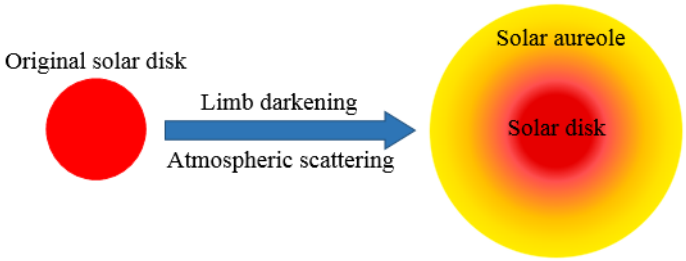

Fig. 2 Schematic of the sunshape

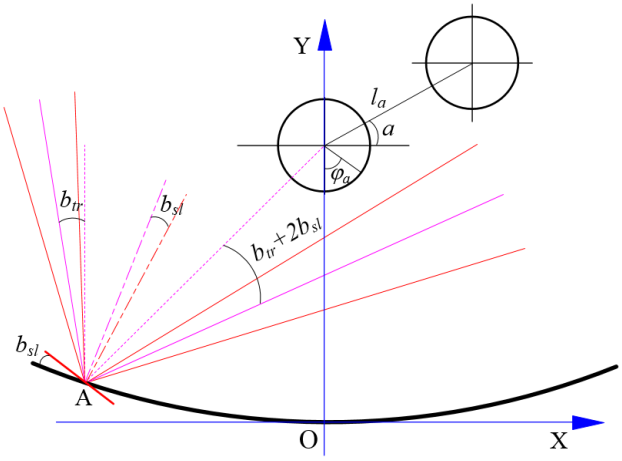

Fig. 3 Geometric description of optical errors (without specularity error)

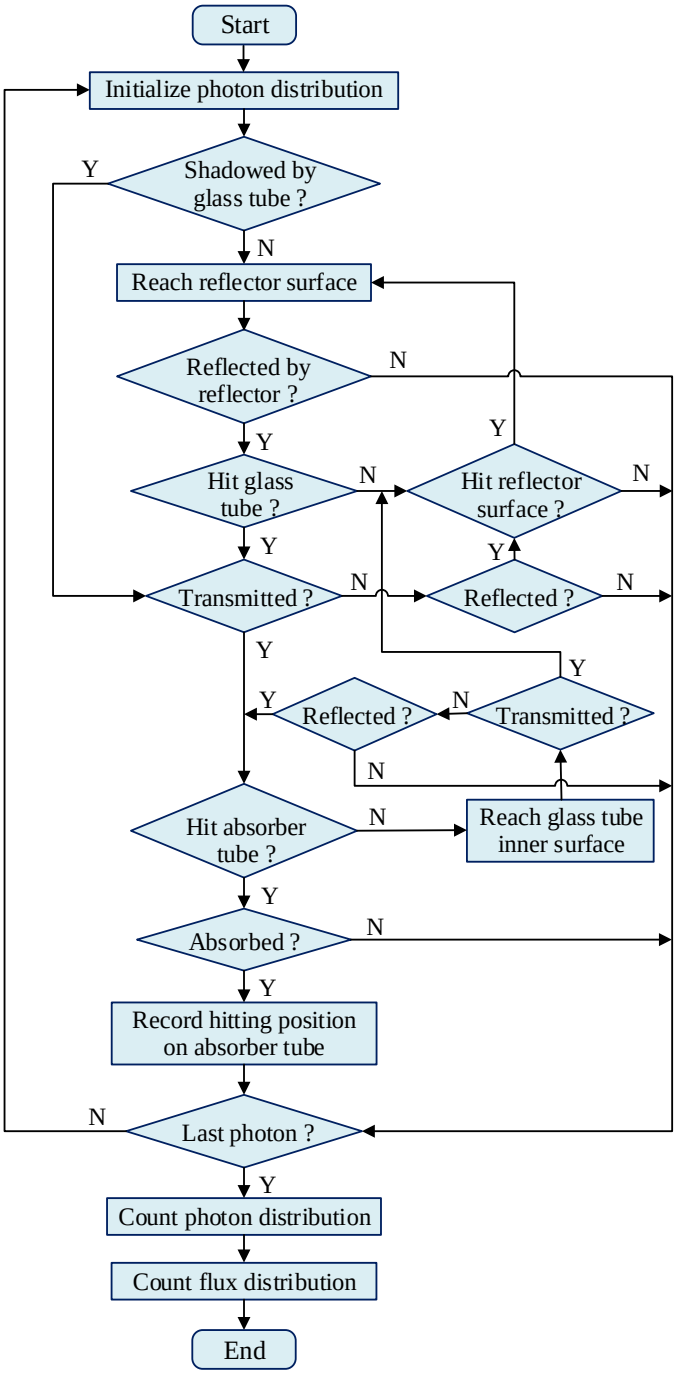

Fig. 4 Flowchart of MCRT

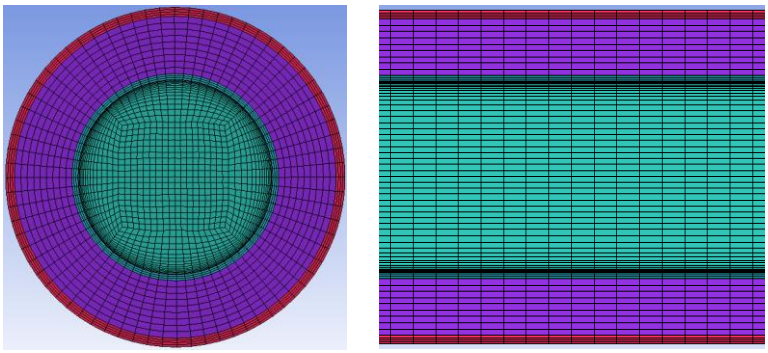

Fig. 5 Schematic of domain discretization (meshing) of the receiver tube

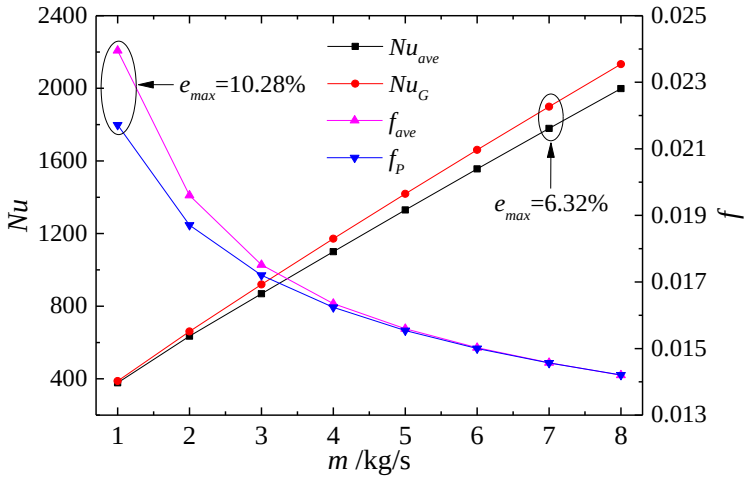

Fig. 6 Comparison of the results between simulation and empirical formulas

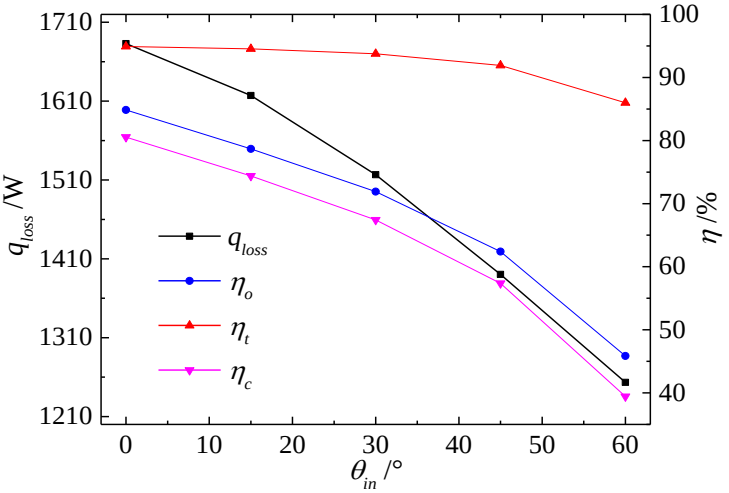

Fig. 7 Variation of heat loss (q_{loss}) and each efficiency (η) with the incident angle (θ_{in})

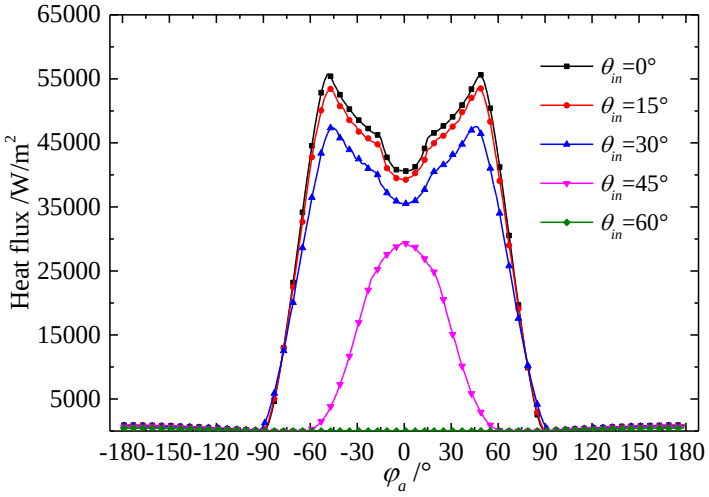

(a)

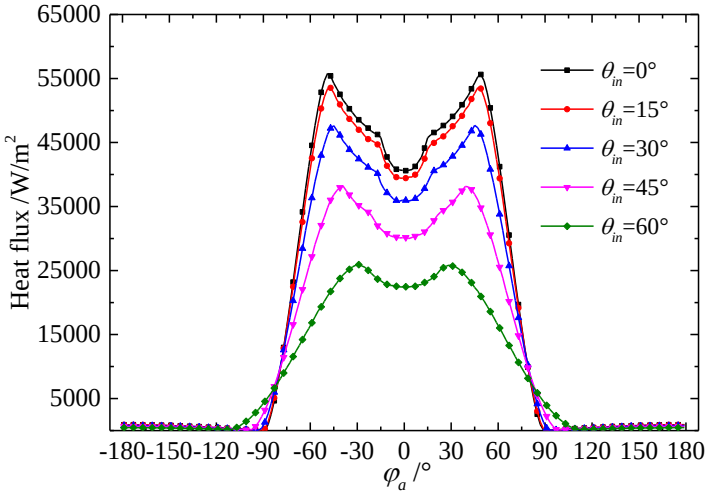

(b)

Fig. 8 Circumferential heat flux distribution on the absorber outer surface under different incident angles (θ_{in}): (a) z=2 m, (b) z=7.5 m

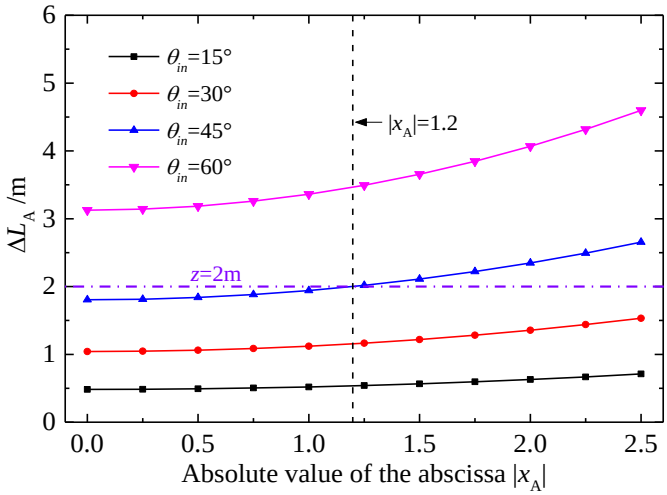

Fig. 9 Variation of ΔL_{A} with the absolute value of abscissa of point A ($|x_{\mathrm{A}}|$) under different incident angles (θ_{in})

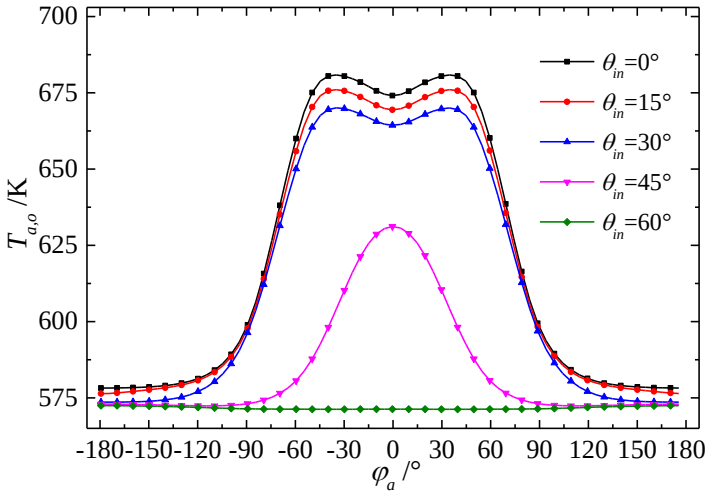

(a)

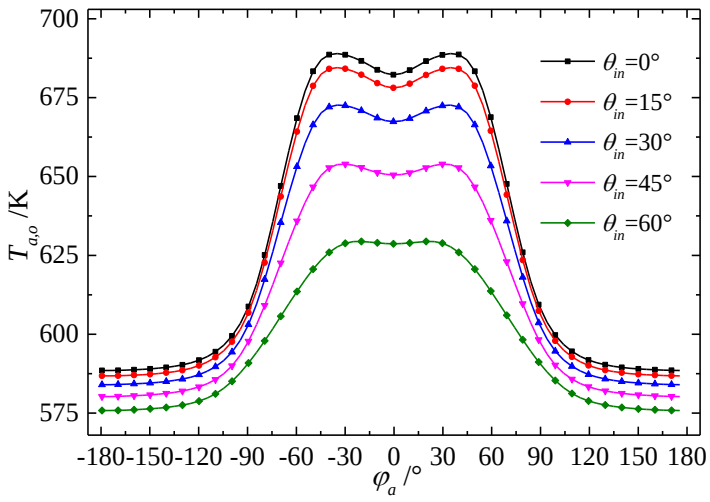

(b)

Fig. 10 Circumferential temperature distribution on the absorber outer surface under different incident angles (θ_{in}): (a) z=2 m, (b) z=7.5 m

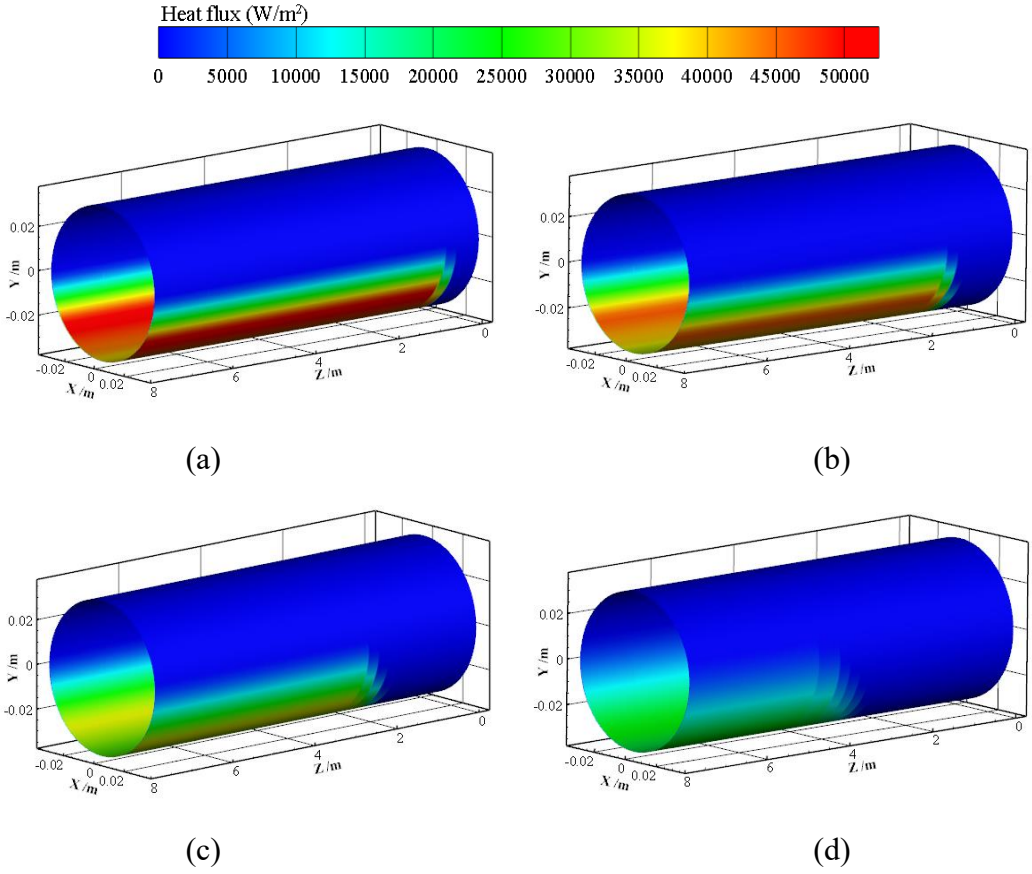

(a) (b)

(c) (d)

Fig. 11 Color map of circumferential heat flux distribution on the absorber outer surface under different incident angles (θ_{in}): (a) θ_{in}=15°, (b) θ_{in}=30°, (c) θ_{in}=45°, (d) θ_{in}=60°

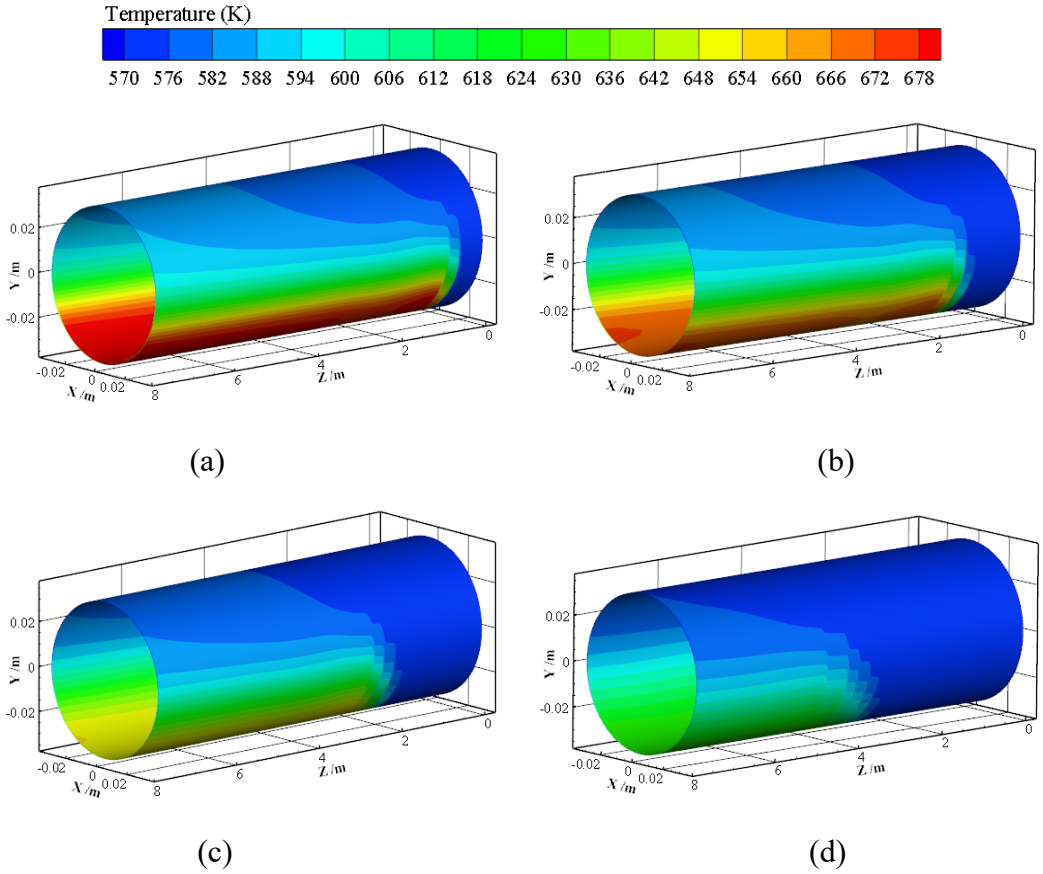

Fig. 12 Color map of circumferential temperature distribution on the absorber outer surface under different incident angles (θ_{in}): (a) θ_{in}=15°, (b) θ_{in}=30°, (c) θ_{in}=45°, (d) θ_{in}=60°

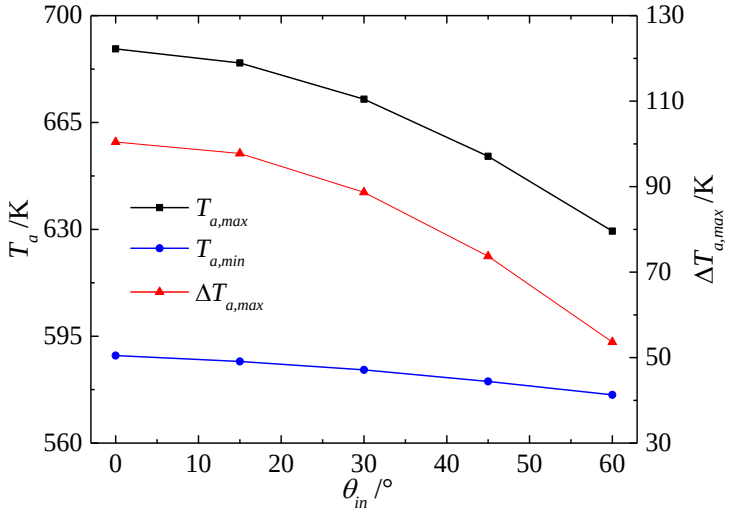

(a)

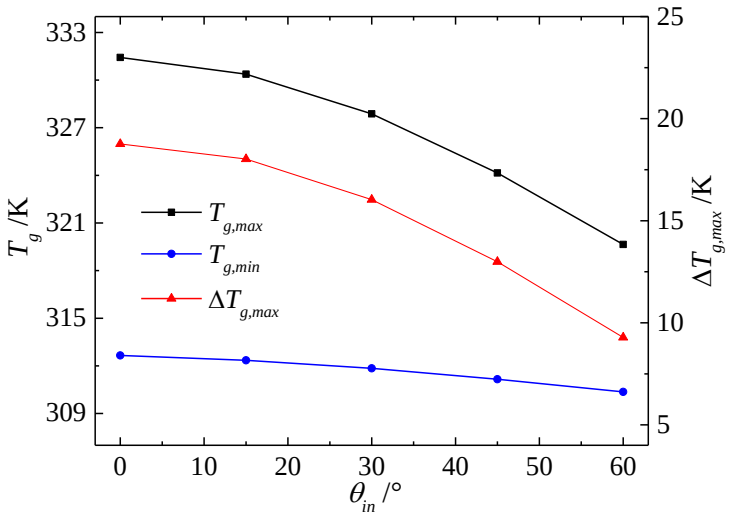

(b)

Fig. 13 Variation of the maximum and minimum temperature and the maximum circumferential temperature difference at z=7.5 m with the incident angle (θ_{in}): (a) absorber tube, (b) glass envelope

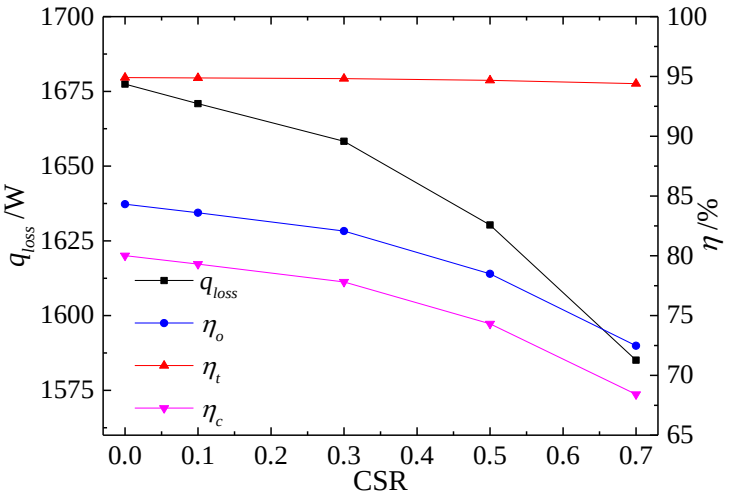

Fig. 14 Variation of heat loss (q_{loss}) and each efficiency (η) with the circumsolar ratio (CSR)

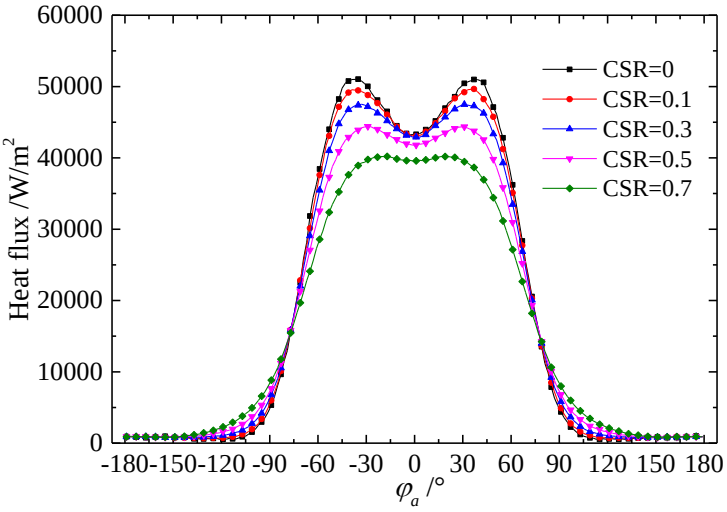

(a)

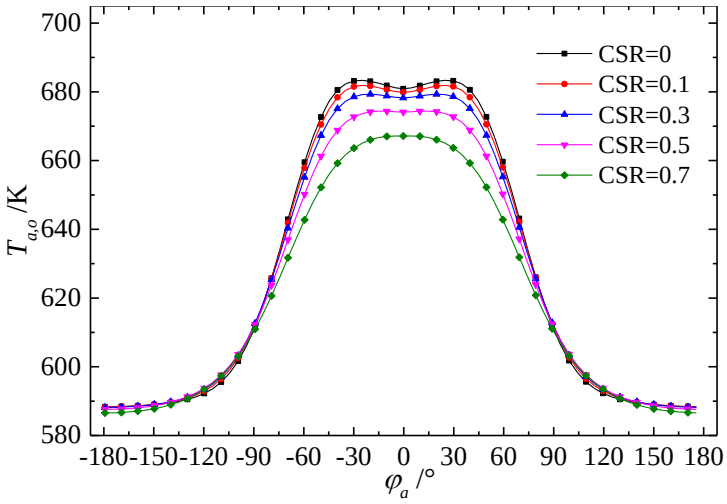

(b)

Fig. 15 Circumferential heat flux and circumferential temperature distribution on the absorber outer surface at z=7.5 m under different circumsolar ratios (CSRs): (a) heat flux distribution (b) temperature distribution

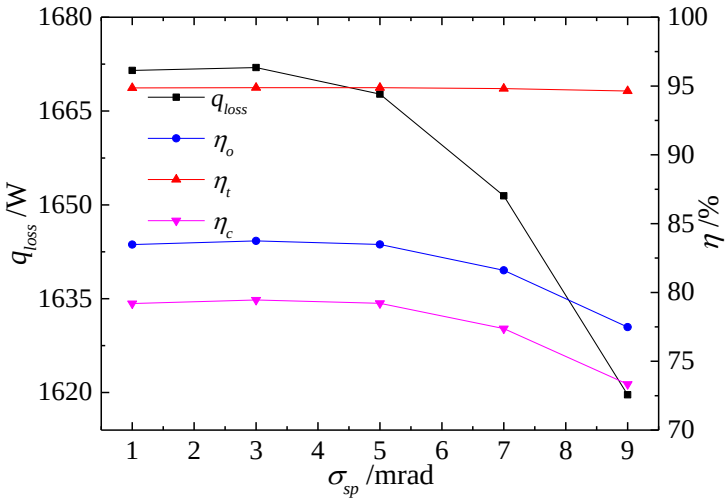

Fig. 16 Variation of heat loss (q_{loss}) and each efficiency (η) with the specularity error (σ_{sp})

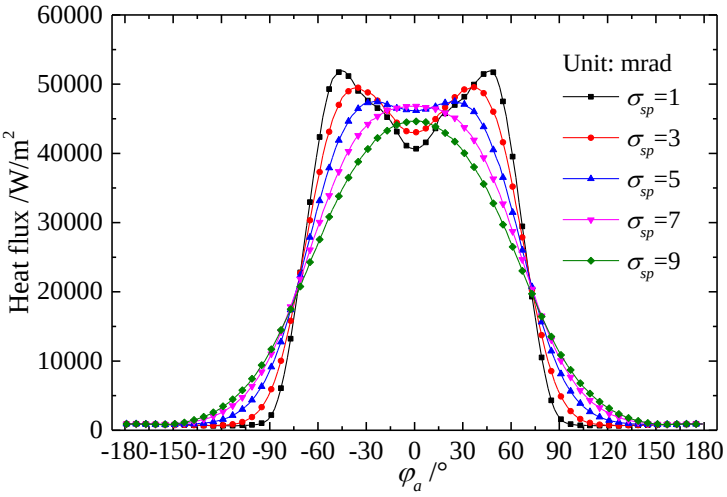

(a)

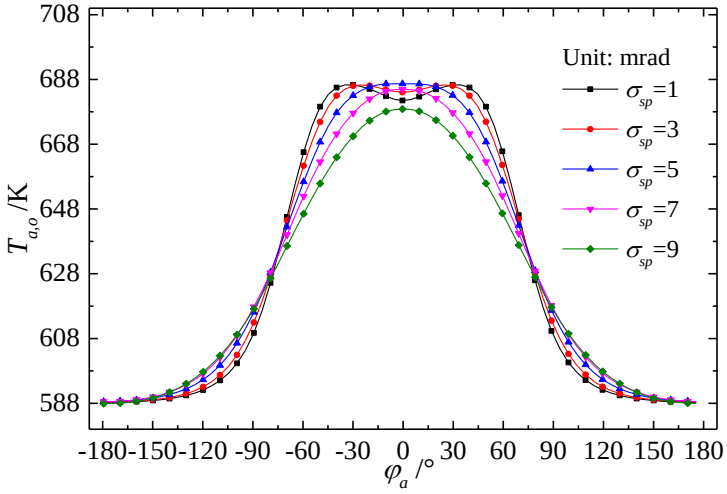

(b)

Fig. 17 Circumferential heat flux and circumferential temperature distribution on the absorber outer surface at z=7.5 m under different specularity errors (σ_{sp}): (a) heat flux distribution (b) temperature distribution

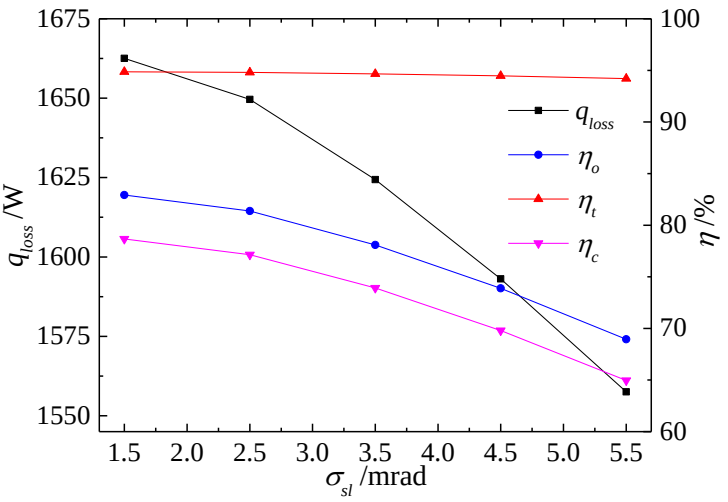

Fig. 18 Variation of heat loss (q_{loss}) and each efficiency (η) with the slope error (σ_{sl})

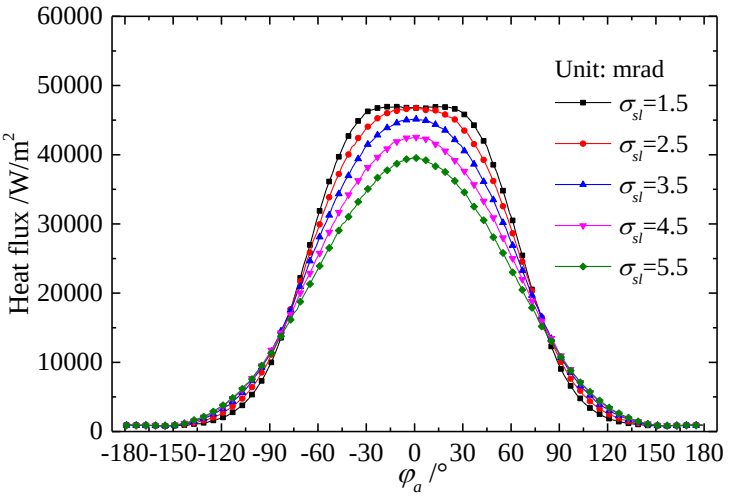

(a)

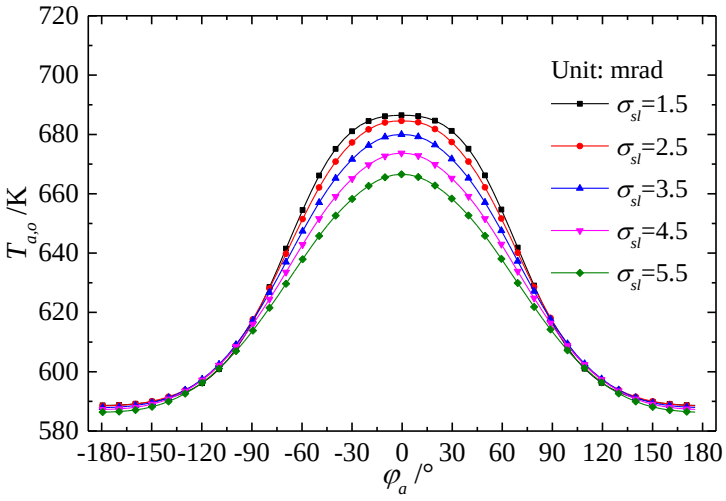

(b)

Fig. 19 Circumferential heat flux and circumferential temperature distribution on the absorber outer surface at z=7.5 m under different slope errors (σ_{sl}): (a) heat flux distribution (b) temperature distribution

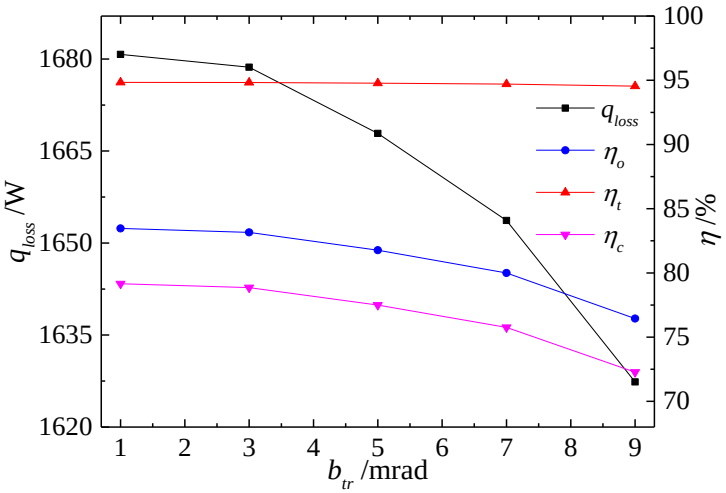

Fig. 20 Variation of heat loss (q_{loss}) and each efficiency (η) with the tracking error (b_{tr})

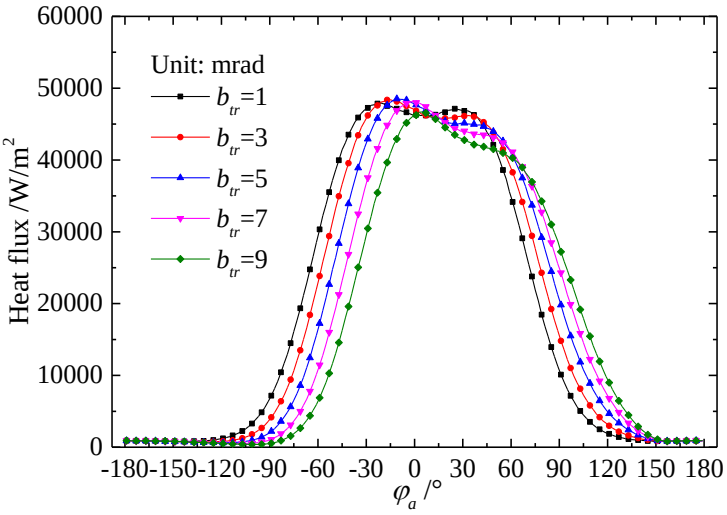

(a)

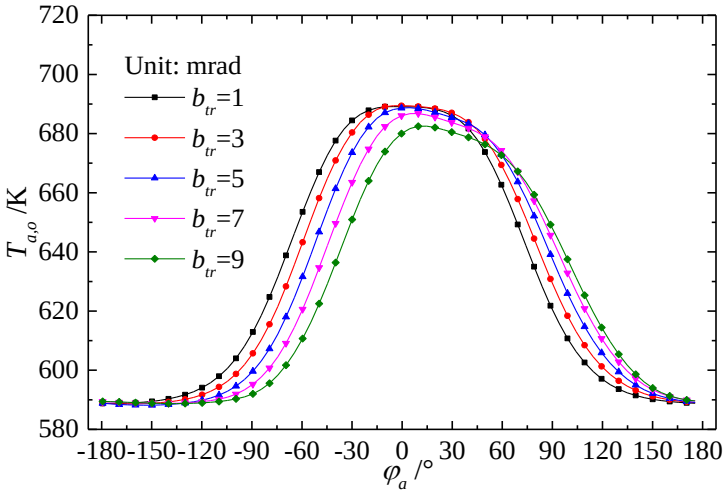

(b)

Fig. 21 Circumferential heat flux and circumferential temperature distribution on the absorber outer surface at z=7.5 m under different tracking errors (b_{tr}): (a) heat flux distribution (b) temperature distribution

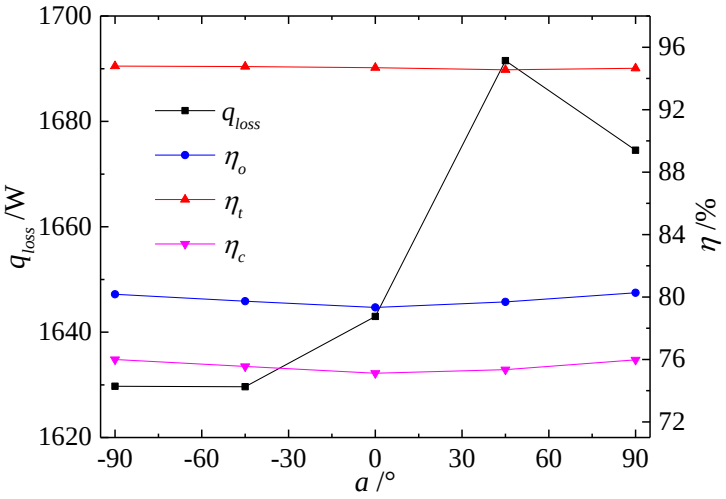

Fig. 22 Variation of heat loss (q_{loss}) and each efficiency (η) with the offset angle (a) in the case of l_a =0.02 m

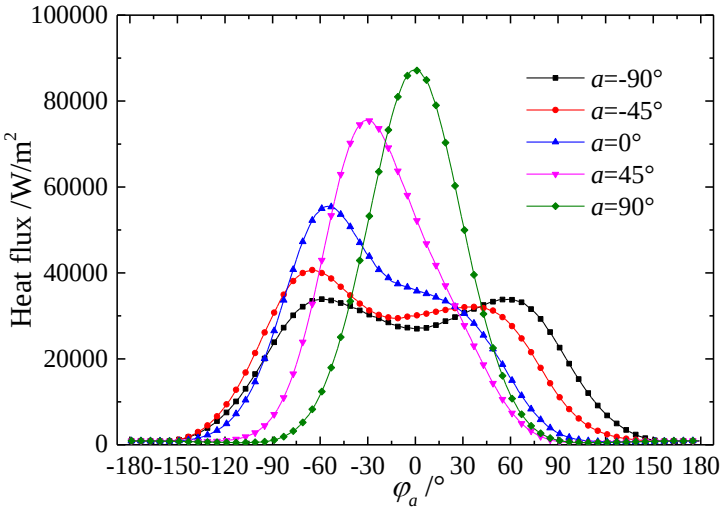

(a)

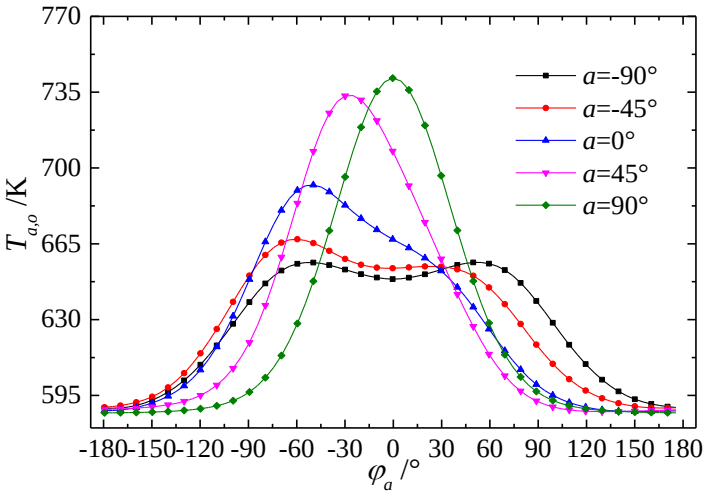

(b)

Fig. 23 Circumferential heat flux and circumferential temperature distribution on the absorber outer surface at z=7.5 m under different offset angles (a) for l_a=0.02 m: (a) heat flux distribution (b) temperature distribution

Tables:

Table 1 Constants in the turbulence model [49]

C_μ	C_1	C_2	σ_k	σ_ε	σ_t
0.09	1.44	1.99	1	1.3	0.85

Table 2 Parameters of SEGS LS-2 PTC module [19]

Parameter	Value	Unit
W_c	5	m
f_c	1.84	m
L_c	7.8	m
$d_{a,o}$	0.07	m
$d_{g,o}$	0.115	m

α_a	0.96	——
ρ_r	0.93	——
τ_g	0.95	——

Table 3 Thermal property parameters of Syltherm 800 [51]

Parameters	Fitting formula
Density (kg/m^3)	$\rho = -6.061657\times10^{-4}T^2 - 0.4153495T + 1105.702$
Specific heat (J/kg·K)	$c_p = 1.708T + 1.107798$
Thermal conductivity (W/m·K)	$\lambda = -5.753496\times10^{-10}T^2 - 1.875266\times10^{-4}T + 0.190021$
Dynamic viscosity (Pa·s)	$\mu = 6.672331\times10^{-13}T^4 - 1.56003\times10^{-9}T^3 + 1.388285\times10^{-6}T^2 - 5.541277\times10^{-4}T + 0.08486612$

Table 4 Typical test data from Ref. [19] for model validation

Case	I_D (W/m^2)	m (kg/s)	V_{amb} (m/s)	T_{amb} (K)	T_{in} (K)	$T_{out,t}$ (K)
1	933.7	0.6782	2.6	294.35	375.35	397.15
2	937.9	0.6206	1.0	301.95	570.95	590.05
3	968.2	0.6536	3.7	295.22	424.15	446.45
4	813.1	0.7254	3.6	298.95	374.35	392.15
5	858.4	0.7207	3.1	300.75	427.45	444.85
6	896.4	0.664	0.9	303.15	523.85	540.95

Table 5 Results for grid independence checking

Grid system	T_{out} (K)	Nu_{ave}	f_{ave}
32×24×500	400.41	70.18	0.0458133
40×30×350	400.05	68.80	0.0458420
40×35×500	399.95	69.98	0.0458481
48×40×350	399.59	69.49	0.0458577
56×45×350	399.52	69.68	0.0458631
72×40×400	399.35	69.65	0.0458636
72×50×400	399.35	69.64	0.0458633
80×55×450	399.35	69.65	0.0458634

Table 6 Comparison of results between simulation and test

Case	T_{in} (K)	$T_{out,t}$ (K)	$T_{out,s}$ (K)	$\lvert T_{out,t} - T_{in} \rvert$ (K)	$\lvert T_{out,s} - T_{out,t} \rvert$ (K)	e_T(%)
1	375.35	397.15	399.35	21.8	2.2	10.09
2	570.95	590.05	591.87	19.1	1.82	9.53
3	424.15	446.45	448.25	22.3	1.8	8.07
4	374.35	392.15	393.88	17.8	1.73	9.92
5	427.45	444.85	446.01	17.4	1.16	6.67
6	523.85	540.95	542.71	17.1	1.74	10.29